LETTER

doi:10.1038/nature14272

Vapour-mediated sensing and motility in two-component droplets

N. J. Cira[1], A. Benusiglio[1] & M. Prakash[1]

Controlling the wetting behaviour of liquids on surfaces is important for a variety of industrial applications such as water-repellent coatings[1] and lubrication[2]. Liquid behaviour on a surface can range from complete spreading, as in the 'tears of wine' effect[3,4], to minimal wetting as observed on a superhydrophobic lotus leaf[5]. Controlling droplet movement is important in microfluidic liquid handling[6], on self-cleaning surfaces[7] and in heat transfer[8]. Droplet motion can be achieved by gradients of surface energy[9–13]. However, existing techniques require either a large gradient or a carefully prepared surface[9] to overcome the effects of contact line pinning, which usually limit droplet motion[14]. Here we show that two-component droplets of well-chosen miscible liquids such as propylene glycol and water deposited on clean glass are not subject to pinning and cause the motion of neighbouring droplets over a distance. Unlike the canonical predictions for these liquids on a high-energy surface, these droplets do not spread completely but exhibit an apparent contact angle. We demonstrate experimentally and analytically that these droplets are stabilized by evaporation-induced surface tension gradients and that they move in response to the vapour emitted by neighbouring droplets. Our fundamental understanding of this robust system enabled us to construct a wide variety of autonomous fluidic machines out of everyday materials.

When droplets of food colouring (containing propylene glycol, PG) are mixed with water and placed on a clean glass slide, they spontaneously move in beautiful and intricate patterns (Fig. 1a and Supplementary Video 1). Here, we first discuss the wetting behaviour of individual droplets, before investigating the multidroplet interactions that cause droplet motion.

We observed that pure water and pure PG spread completely when placed on corona-discharge-cleaned glass slides (Supplementary Information section 1). This is expected on such a high-energy surface for which the spreading parameter, defined as $S = \gamma_{SV} - (\gamma_{LV} + \gamma_{SL})$, is larger than zero, where γ represents the surface energy of the solid/vapour, liquid/vapour, and solid/liquid interfaces[15]. Surprisingly, mixtures of PG and water formed droplets with apparent contact angles θ_{app}, even though $S \geq 0$. The trend in θ_{app} went from zero to a maximum value and back to zero as PG was added to water (Fig. 2a), which cannot be explained simply by the monotonically decreasing liquid/vapour surface tension (Extended Data Fig. 1)[16]. Breathing onto a droplet noticeably modified the contact angle. To quantify this observation, we deposited droplets in controlled humidity chambers and found that apparent contact angle decreased with relative humidity (RH), and droplets spread under saturated RH (Fig. 2b), suggesting that vapour affects droplet stabilization.

Using tracer beads (1 μm diameter) we visualized an internal flow from centre to edge along the bottom of the droplet, similar to the flow in the 'coffee ring' effect[17]. We also observed a flow from the edge to the centre along the top of the droplet, at higher velocity than the outward

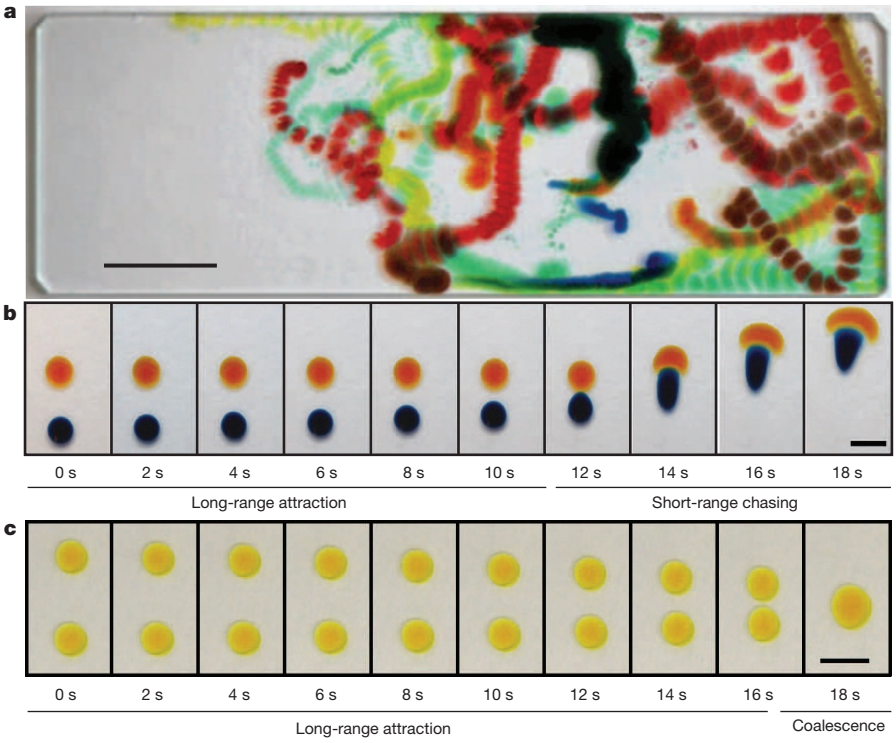

Figure 1 | Long-range and short-range interactions in two-component droplets. **a**, Overlaid time lapse image of multiple coloured droplets deposited on a corona-discharge-cleaned glass slide interacting autonomously for 2 min (see Supplementary Video 1, part 1; scale bar, 10 mm). **b**, Two 0.5 μl droplets of 25% PG (blue) and 1% PG (orange) interacting. The behaviour can be divided into 'long-range attraction' and 'short-range chasing' portions (see Supplementary Video 1, part 2; scale bar, 3 mm). **c**, Two droplets of exactly the same concentration (0.5 μl 10% PG) also attract each other, through long-range interaction followed by coalescence. All percentage PG values are given as volume percentages (volume of PG divided by total volume). (See Supplementary Video 1, part 3; scale bar, 5 mm.)

[1]Department of Bioengineering, Stanford University, 450 Serra Mall, California 94305, USA.

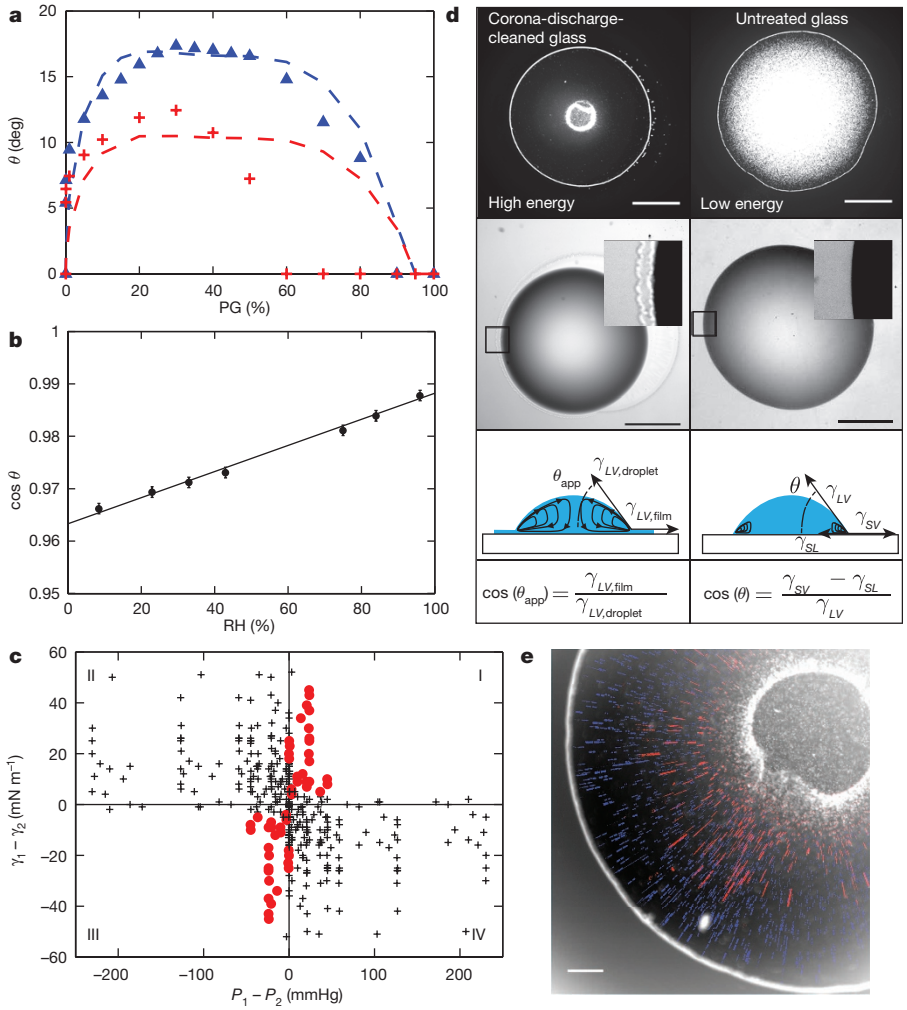

Figure 2 | Individual droplet characteristics. **a**, Isolated droplets (0.5 µl) on a clean glass surface display a non-monotonic apparent contact angle as a function of percentage PG. Crosses and triangles indicate data taken at 75% RH and 40% RH, respectively. Dashed lines indicate the model's fit to the data. **b**, The cosine of the apparent contact angle varies linearly (line of best fit shown) with external humidity (RH) for 0.5 µl 10% PG droplets. Error bars are the range of three measurements at 75% RH. **c**, Behaviour of two-component mixtures of all nonreactive combinations of 21 miscible fluids (see Supplementary Table 1 for chemical list) on corona-discharge-cleaned glass. For each liquid pair, difference in surface tension γ is plotted against difference in vapour pressure P. Red dots indicate droplet formation and black crosses indicate complete wetting. **d**, Important differences between two-component droplets deposited on high- and low-energy solid substrates. From top to bottom: accumulation of beads at the liquid/vapour interface, visualization of the thin film (contrast is enhanced in the insets, which magnify the boxes) (scale bars, 1 mm), flow representation (diagram), and force equilibrium (equation). **e**, Time-lapse trajectories of tracer beads in the droplet. Red traces are focused at the top surface where beads move towards the centre, while blue traces are in the plane close to the glass where beads move outward (scale bar, 200 µm).

flow (Fig. 2d and e). This less commonly seen 'counter flow' has been observed with surfactant or thermal gradients only in pinned droplets[18,19]. It collects tracer beads at the liquid–vapour interface into a prominent ring (Fig. 2e). Experiments with multiple chemical combinations on multiple substrates demonstrate that thermocapillarity does not appear to be a substantial driving force in our system (Extended Data Figs 2 and 3; Supplementary Information section 2.5). Microscopic observation of the droplets revealed a thin film extending tens of micrometres from the edge of the bulk droplet into which the 1 µm tracer beads did not enter (Fig. 2d, Supplementary Video 2). For the same droplets on a lower-energy surface the counter flow was confined to the border of the droplet (Fig. 2d). No tracer bead ring appeared (Supplementary Video 2), there was no thin film around the droplets, and the droplets were less mobile and did not interact.

From these observations we can understand the mechanism that prevents complete spreading. The high-energy surface favours spreading of the droplet, as seen for pure liquids[20]. For a two-component droplet of water and PG, the more volatile compound (water) evaporates more quickly than the less volatile compound (PG). Evaporation is faster at the border of the droplet than the bulk[17], and the border of the droplet has a higher surface area to volume ratio. Therefore PG, with a lower γ_{LV} than water, is left in higher concentration at the border than the bulk. The resulting gradient of surface tension, or so called Marangoni stress, pulls liquid towards the centre along the top of the droplet, an effect shown to slow down or stop spreading[2,21,22]. Here the spreading is stopped, resulting in a droplet with a stable apparent contact angle θ_{app} (Extended Data Fig. 4) surrounded by a thin film (Figs 2d and 3a)[2].

Next, we built a simple model to test this mechanism of droplet stabilization. We assumed a sharp transition of surface tension between the bulk droplet ($\gamma_{LV,\,droplet}$) and the surrounding thin film ($\gamma_{LV,\,film}$). We introduced a quasi-static horizontal force balance at the intersection of the thin film and the bulk droplet, $\gamma_{LV,\,droplet}\cos(\theta_{app}) = \gamma_{LV,\,film}$. To calculate θ_{app}, we modelled the water loss from the thin film due to evaporation, estimating the water fraction and surface tension of the film as a function of both the external RH and water fraction of the droplet (Supplementary Information section 2.3, Extended Data Figs 5 and 6). Using this model we fitted a single parameter for 40% RH and observed that the prediction globally captures the non-monotonic contact angle curve and accounts for variation in this curve as a function of RH (Fig. 2a). Our current model accounts only for water evaporation, and is therefore less accurate at high PG concentration and high RH.

Based on this model, for any two miscible chemicals on a high-energy substrate, droplets should form if and only if one of the chemicals in the mixture has both a higher surface tension and higher vapour pressure (quadrants I and III in Fig. 2c). To test this law, we placed various two-component mixtures on corona-discharge-cleaned glass slides. In about 200 unique combinations (Extended Data Table 1), droplet formation versus spreading was well predicted, excluding reactive pairs (Fig. 2c), and these droplets had attributes similar to those of the PG/water system, such as high mobility and interactions. We also deposited PG/water droplets on other high-energy substrates—piranha-treated glass, flamed glass, clean silicon wafers, freshly scraped steel, flamed aluminium, and plasma-oven-treated flexible indium tin oxide (ITO)-coated polyethylene terephthalate (PET)—and found similar behaviour.

These two-component droplets have characteristics of both wetting and non-wetting liquids: they maintain a defined contact angle but sit on a thin fluid film. As long as $S \geq 0$, the droplets should not 'feel' the solid surface, and chemical inhomogeneities and roughness should not

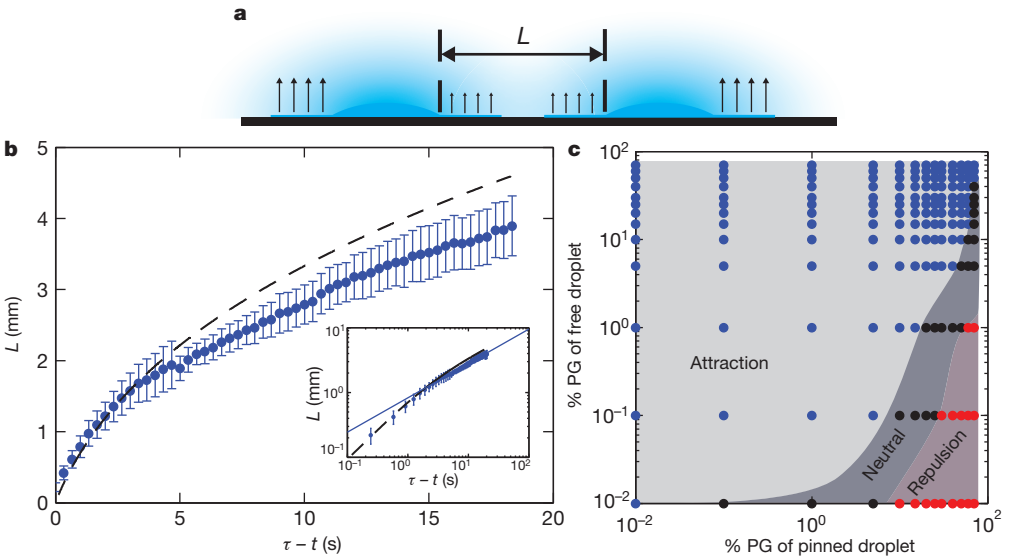

Figure 3 | Long-range droplet interactions. **a**, Schematic of vapour gradients (blue shading) and evaporation (upward arrows) from two droplets a distance L apart. Increased vapour concentration between the droplets leads to less evaporation. **b**, Mean distance between droplets as a function of time before contact for two freely moving 0.5 µl 10% PG droplets. The error bars represent the standard deviation of 12 experiments, and the dashed line is the model prediction. The inset shows the log-log scale of the same data, with solid line as the power-law fit. τ is the time of droplet contact. **c**, Phase diagram of interactions between a single pinned and a single free 0.5 µl droplet (the axes show percentage by volume of PG). Each dot represents an experiment; each colour indicates the direction of motion of the free droplet.

cause pinning. The droplet contact angle is also independent of the substrate (γ_{SV}) and surface roughness. Without pinning, the droplets display high mobility and hence move under the influence of minute forces (<1 µN, Extended Data Fig. 7). We do not observe high mobility on low-energy surfaces with a three-phase contact line, where high hysteresis limits droplet motion.

When two droplets were deposited at distances of up to several radii apart, they moved towards each other; this occurred over a wide range of concentrations, even when both droplets had the same concentration (Figs 1b and c, and 3c). Droplets increased speed as they approached each other (Fig. 3b). These long-range interactions were preserved even across a break in the glass slide (Supplementary Video 3, part 1). PG/water droplets followed a pipette tip containing water placed near to but not touching the droplet or the glass slide (Supplementary Video 3 Part 2). These observations and our measurements of θ_{app} versus RH (Fig. 2b) led us to the surprising conclusion that long-range interactions were vapour-mediated.

From the observations above, we propose a mechanism for vapour-mediated interactions different from mechanisms proposed in other systems[23,24]. Evaporation from a sessile droplet is known to produce a vapour gradient[25]. Since the vapour pressure of water is one hundred times larger than the vapour pressure of PG, the dominant vapour is water. Two neighbouring droplets each lie in a gradient of water vapour produced by the other (Fig. 3a). This gradient causes a local increase in RH and thus decreased evaporation of the thin film on the adjacent portions of the droplets, breaking symmetry. The decreased evaporation leads to an increased water fraction in the thin film, hence increasing $\gamma_{LV,\,film}$ locally. Asymmetric $\gamma_{LV,\,film}$ around the droplet causes a net force that drives the droplets towards each other.

To test this mechanism, we propose a mathematical model to calculate the expected distance L between two identical droplets as a function of time (Fig. 3a, Supplementary Information section 2.4). We start with the diffusion equation to estimate the local RH profile around a droplet. By using our prior measurements of θ_{app} of a static droplet as a function of uniform external RH, we estimate the local $\gamma_{LV,\,film}$ around each droplet as a function of the local RH imposed by the other droplet. Integrating $\gamma_{LV,\,film}$ around the edge we obtain the net force acting on each droplet as $F_{net} = 2\gamma_{LV,\,droplet} mR \int_0^{\pi} \left(\frac{(1-\mathrm{RH}_{room})R\cos(\psi)}{\sqrt{d^2+R^2+2Rd\cos(\psi)}} \right) \mathrm{d}\psi$, where m is the slope of $\cos(\theta_{app})$ plotted versus RH (Fig. 2b), R is the radius of the droplet, d is the distance between the droplet centres, ψ is the parameter of integration, and RH_{room} is the ambient humidity far from the droplets. This net force causes droplet motion and is balanced by a viscous drag force, F_{drag}. Here we neglect inertia since the Reynolds number, Re, is smaller than 1 (for typical droplet velocity 1 mm s^{-1} and droplet radius 1 mm, Re ≈ 0.3).

We calibrated F_{drag} by measuring droplet speed on ramps of known angle, observing that it scaled linearly with the velocity U as $F_{drag} = C_{drag}U$ (Extended Data Fig. 8). The drag coefficient C_{drag} was a linear function of the droplet perimeter, consistent with existing theory based on viscous dissipation at three-phase contact lines[26] (Supplementary Information Section 2.1 and 2.2, Extended Data Figs 7 and 8). Equating F_{drag} with F_{net}, we obtain and integrate the instantaneous velocity to arrive at the distance between the two droplets, $L(t)$. Plotting L as a function of $\tau - t$ with τ as the time of droplet contact, we observe a good agreement between model and data, with no adjustable parameters (Fig. 3b). In a log-log plot $L(\tau - t)$ behaves as a scaling law of exponent 0.6 at long distance, which is also captured by the model (inset to Fig. 3b).

In Fig. 3c, we present a phase diagram of long-range interactions between one pinned droplet and one mobile droplet, as a function of concentration of both droplets. Over a large concentration range the mobile droplet was attracted to the pinned droplet. However, when $[\mathrm{PG}]_{pinned} \gg [\mathrm{PG}]_{mobile}$, the mobile droplet fled, indicating a repulsive force. We hypothesize that at high PG concentration, the gradient of the PG vapour begins to contribute to long-range motion, decreasing $\gamma_{LV,\,film}$ and driving the mobile droplet away.

At short range, two droplets of like concentrations coalesce upon contact. Droplets of sufficiently different concentrations can undergo a prolonged 'chasing phase'[23] as recently explained[27,28] (Fig. 1b). Fluid is directly exchanged between the droplets, as visualized by a fluorescent dye (Supplementary Video 4). This exchange of fluid leads to a surface tension gradient and Marangoni flow across both the droplets, where the droplet of lower surface tension 'chases' the droplet of higher surface tension, which in turn 'flees' away[28]. Additional subtleties of short-range interactions can be obtained by adjusting concentrations and volumes (Supplementary Information; Extended Data Fig. 9).

Using the fundamental understanding we developed for this system, we explored several applications by building multiple self-fuelled surface-tension-driven fluidic machines out of everyday materials such as food colouring, glass slides, and permanent Sharpie marker (Supplementary Information section 1.5). First, we used the long-range interactions to create a droplet self-aligner, which aligns randomly placed droplets of identical concentrations in different 'lanes' into a single straight line

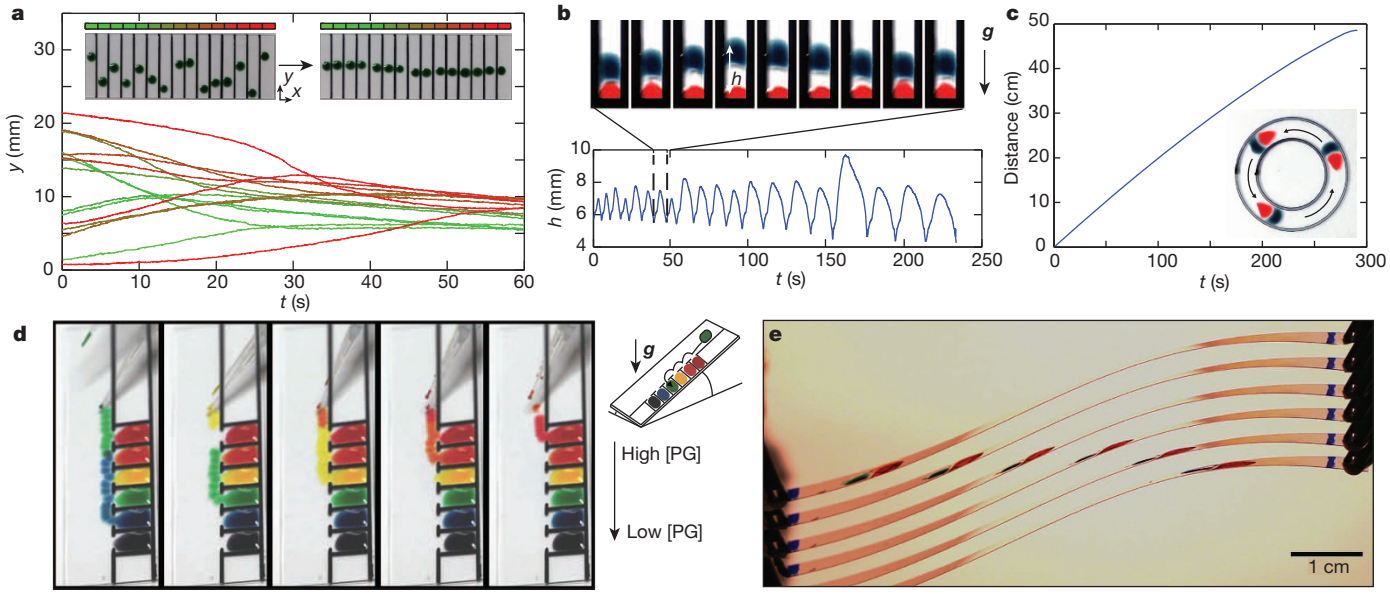

Figure 4 | Droplet-based devices. We created four devices by drawing permanent marker (Sharpie, black) lines, which are hydrophobic enough that droplets do not cross them (Supplementary Video 5, parts 1–3 and Supplementary Video 6). **a**, Spontaneous droplet aligner. Upper left inset shows 0.5 µl green droplets of 10% PG dispensed at random initial positions separated by 5 mm spaced Sharpie lines. Upper right inset shows the droplets automatically aligned into final positions. The graph shows the *y* position of each droplet as a function of time. The colour code represents the *x* position in the aligner. **b**, Vertical droplet oscillator. We deposited a 25% PG droplet (blue) above a 1% PG droplet (red) bounded in a 4 mm lane on a vertical glass slide. The top droplet oscillates up and down. The top panel shows one oscillation, with images separated by 1 s. The direction of the gravitational acceleration is shown by *g*, and the bottom panel shows the vertical position *h* of the top droplet as a function of time. **c**, Circular chasing. Short-range chasing between a 1% PG droplet (red) and a 25% PG droplet (blue) in a circle of mean diameter 2.1 cm. The inset shows a three-image time lapse (10 s spacing, arrows representing direction of motion). The graph shows the travelled distance as a function of time. **d**, Surface tension sorter. The schematic shows wells of various concentrations of PG (colours) confined by Sharpie lines (black). Concentrations from top to bottom are 30% PG, 25% PG, 20% PG, 15% PG, 10% PG and 5% PG. Each image shows the time-lapse trajectory of a droplet as it is deposited at the top and moves down under gravity, sampling each well, but merging only with a well of like concentration. Sorting happens purely passively. **e**, Flexible substrate. We demonstrate droplet chasing on a flexible plasma-oven-treated ITO/PET strip. The image was compiled by offsetting six frames from Supplementary Video 5, part 4.

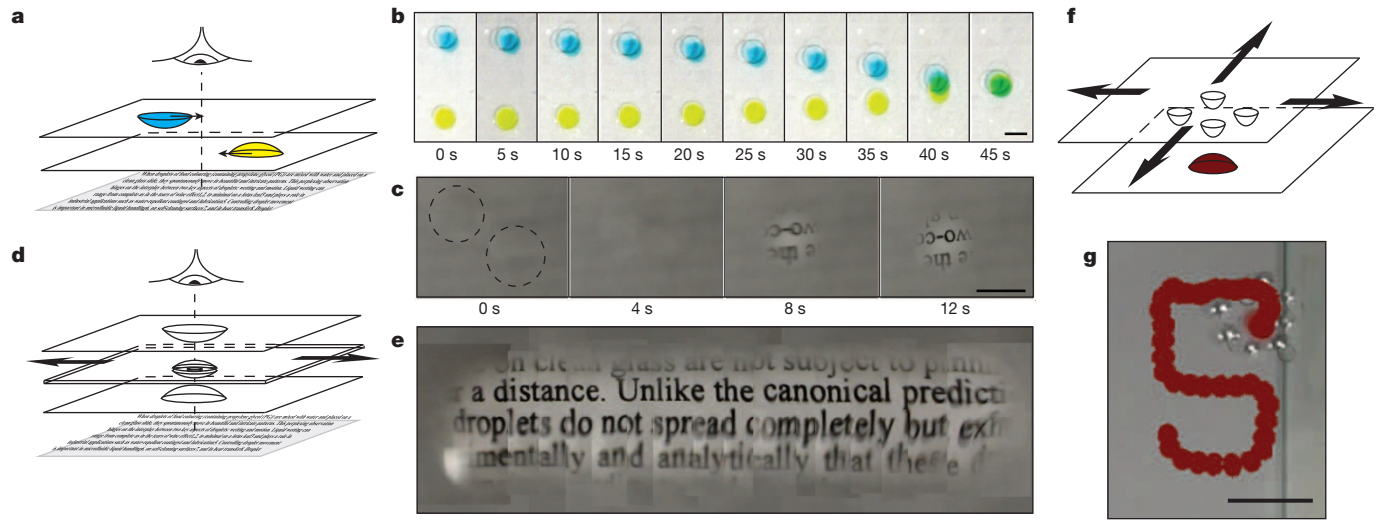

Figure 5 | Droplet-based devices using parallel plates. **a**, We created devices where droplets interacted with each other via vapour across a gap between parallel glass slides (Supplementary Videos 7 and 8). **b**, Time-lapse dynamics of interaction (0.5 µl 10% PG droplets, yellow on bottom slide, blue on top; scale bar, 4 mm). **c**, A self-assembling, self-aligning liquid lens system that forms an image when the top and bottom lenses align (scale bar, 4 mm). **d**, Schematic of a self-assembling, self-aligning three-lens system. The system is the same as the two-lens version with a third plate inserted in the middle. This plate has a drilled hole containing an additional liquid lens pinned in the hole (presenting two new optical surfaces) to which the other lenses align. **e**, An image made by scanning the three-lens assembly across text. As the centre plate was moved, the other lenses followed and aligned, allowing imaging over an area much larger than the lenses (image created by stitching together frames of Supplementary Video 8, part 3). **f**, A schematic of the long-range remote droplet positioning system. Droplets of PG act in long-range repulsion, and when arranged in a ring, these PG droplets create a vapour trap that pushes the PG/water droplet on the other slide to the centre of the trap. **g**, A time-lapse image illustrating remote control of droplet position. The top slide containing the PG vapour trap was moved to create contactless motion of the red droplet on the other slide.

(Fig. 4a, Supplementary Video 5, part 1). Second, we used the short-range interactions to create sustained droplet chasing, during which droplets circled around a single loop for several minutes (Fig. 4c, Supplementary Video 5, part 2). We note that since the droplets do not consume the surface, they are unaffected by prior trajectories and are able to repeatedly cross over their own paths. Third, we created a completely vertical droplet oscillator by placing a large low-surface-tension droplet beneath a higher-surface-tension droplet bounded in a lane on a glass slide (Fig. 4b, Supplementary Video 5, part 3). By changing the device parameters, the droplets were able to sustain chasing over the length of the slide against gravity (droplets run up a vertical wall). We also demonstrate short-range chasing on flexible ITO/PET, enabling applications for three-dimensional curved substrates (Fig. 4e, Supplementary Video 5, part 4). Finally, we demonstrate a new method for self-sorting droplets based on small surface tension differences. In this device, we relied on gravity to bring droplets down a ramp, where they sampled wells from low to high surface tension, merging only when they reached a like concentration, effectively sorting themselves into bins (Fig. 4d, Supplementary Video 6).

We further explored the application of long-range interactions by introducing a parallel plate geometry that allows droplet communication across disparate substrates via long-range interactions. We placed droplets on the adjacent sides of parallel glass slides separated by gaps of 0.15 mm to 4 mm (Fig. 5a). This parallel plate configuration resulted in prolonged droplet interaction, since evaporation was reduced by the additional boundary. Since the vapour gradient is more gradual in two dimensions, droplets also interacted over larger distances. We created several devices in this configuration. First, we made a contactless remote droplet positioning system based on long-range repulsion (Fig. 2f) by placing pinned droplets of pure PG in a ring on one slide and using them to manipulate mobile droplets on the other slide, creating a 'vapour trap' (Fig. 5g, Supplementary Video 7). Second, we noted that long-range attraction vertically aligns droplets on opposite plates (Fig. 5b, Supplementary Video 8, part 1). We exploited this mechanism to make self-assembling, self-aligning fluidic lens systems. These droplet lenses found each other from several lens diameters apart and self-aligned to produce a focused image (Fig. 5c, Supplementary Video 8, part 2). The magnification can be tuned by changing the spacing of optical components and the radius of curvature of the lenses (dictated by contact angle, modulated by concentration and RH as shown in Fig. 2a and b). Finally, we show how to build a self-assembled optical system with four tuneable lens surfaces by inserting a third plate with a hole drilled through it containing a pinned droplet between the two plates with mobile lenses (Fig. 5d). By moving the pinned lens, the entire optical assembly was capable of scanning a wide area (Fig. 5e, Supplementary Video 8, part 3).

These examples illustrate the wide variety of autonomous sensing and motility-based devices that can be created using our system. The system's robustness and ease of reproducibility (Supplementary Video 9) will be useful in further explorations in studying multi-body interactions[29], minimal systems of sensing and actuation, and as a physical analogue for the migration of keratocytes[30] and chemotaxing cells[31].

Online Content Methods, along with any additional Extended Data display items and Source Data, are available in the online version of the paper; references unique to these sections appear only in the online paper.

Received 14 August 2014; accepted 26 January 2015.
Published online 11 March 2015.

1. Wenzel, R. N. Resistance of solid surfaces to wetting by water. *Ind. Eng. Chem.* **28,** 988–994 (1936).
2. Bascom, W. D., Cottington, R. L. & Singleterry, C. R. Dynamic surface phenomena in the spontaneous spreading of oils on solids. http://pubs.acs.org/doi/abs/10.1021/ba-1964-0043.ch026, DTIC document number NRL-5963 (Naval Research Laboratory, 1963).
3. Thomson, J. On certain curious motions observable at the surfaces of wine and other alcoholic liquors. *Phil. Mag.* **10,** 330 (1855).
4. Marangoni, C. Über die Ausbreitung der Tropfen einer Flüssigkeit auf der Oberfläche einer anderen. *Ann. Phys.* **219,** 337–354 (1871).
5. Barthlott, W. & Neinhuis, C. Purity of the sacred lotus, or escape from contamination in biological surfaces. *Planta* **202,** 1–8 (1997).
6. Pollack, M. G., Fair, R. B. & Shenderov, A. D. Electrowetting-based actuation of liquid droplets for microfluidic applications. *Appl. Phys. Lett.* **77,** 1725–1726 (2000).
7. Zhang, X., Shi, F., Niu, J., Jiang, Y. G. & Wang, Z. Q. Superhydrophobic surfaces: from structural control to functional application. *J. Mater. Chem.* **18,** 621–633 (2008).
8. Daniel, S., Chaudhury, M. K. & Chen, J. C. Fast drop movements resulting from the phase change on a gradient surface. *Science* **291,** 633–636 (2001).
9. Chaudhury, M. K. & Whitesides, G. M. How to make water run uphill. *Science* **256,** 1539–1541 (1992).
10. Ichimura, K., Oh, S. K. & Nakagawa, M. Light-driven motion of liquids on a photoresponsive surface. *Science* **288,** 1624–1626 (2000).
11. Gallardo, B. S. *et al.* Electrochemical principles for active control of liquids on submillimeter scales. *Science* **283,** 57–60 (1999).
12. Brzoska, J. B., Brochard-Wyart, F. & Rondelez, F. Motions of droplets on hydrophobic model surfaces induced by thermal gradients. *Langmuir* **9,** 2220–2224 (1993).
13. Style, R. W. *et al.* Patterning droplets with durotaxis. *Proc. Natl Acad. Sci. USA* **110,** 12541–12544 (2013).
14. Dettre, R. H. & Johnson, R. E. Contact angle hysteresis. IV. Contact angle measurements on heterogeneous surfaces. *J. Phys. Chem.* **69,** 1507–1515 (1965).
15. de Gennes, P.-G., Brochard-Wyart, F. & Quéré, D. *Capillarity and Wetting Phenomena: Drops, Bubbles, Pearls, Waves* (Springer, 2004).
16. Hoke, B. C. & Patton, E. F. Surface tensions of propylene-glycol plus water. *J. Chem. Eng. Data* **37,** 331–333 (1992).
17. Deegan, R. D. *et al.* Capillary flow as the cause of ring stains from dried liquid drops. *Nature* **389,** 827–829 (1997).
18. Truskett, V. & Stebe, K. J. Influence of surfactants on an evaporating drop: Fluorescence images and particle deposition patterns. *Langmuir* **19,** 8271–8279 (2003).
19. Hu, H. & Larson, R. G. Analysis of the effects of Marangoni stresses on the microflow in an evaporating sessile droplet. *Langmuir* **21,** 3972–3980 (2005).
20. Tanner, L. H. Spreading of silicone oil drops on horizontal surfaces. *J. Phys. D* **12,** 1473–1484 (1979).
21. Bernett, M. K. & Zisman, W. A. Prevention of liquid spreading or creeping. Contact angle, wettability and adhesion. *Adv. Chem. Ser.* **43,** 332–340 (1964).
22. Pesach, D. & Marmur, A. Marangoni effects in the spreading of liquid mixtures on a solid. *Langmuir* **3,** 519–524 (1987).
23. Bangham, D. H. & Saweris, Z. The behaviour of liquid drops and adsorbed films at cleavage surfaces of mica. *Trans. Faraday Soc.* **34,** 0554–0569 (1938).
24. Carles, P. & Cazabat, A. M. Spreading involving the Marangoni effect—some preliminary results. *Colloids Surf.* **41,** 97–105 (1989).
25. Hu, H. & Larson, R. G. Evaporation of a sessile droplet on a substrate. *J. Phys. Chem. B* **106,** 1334–1344 (2002).
26. Brochard, F. Motions of droplets on solid surfaces induced by chemical or thermal gradients. *Langmuir* **5,** 432–438 (1989).
27. Karpitschka, S. & Riegler, H. Quantitative experimental study on the transition between fast and delayed coalescence of sessile droplets with different but completely miscible liquids. *Langmuir* **26,** 11823–11829 (2010).
28. Riegler, H. & Lazar, P. Delayed coalescence behavior of droplets with completely miscible liquids. *Langmuir* **24,** 6395–6398 (2008).
29. Saha, S., Golestanian, R. & Ramaswamy, S. Clusters, asters and collective oscillations in chemotactic colloids. *Phys. Rev. E* **89,** 062316 (2014).
30. Theriot, J. A. & Mitchison, T. J. Actin microfilament dynamics in locomoting cells. *Nature* **352,** 126–131 (1991).
31. Berg, H. C. E. coli *in Motion* (Springer, 2004).

Supplementary Information is available in the online version of the paper.

Acknowledgements We thank all members of the Prakash Laboratory for discussions. We thank J. C. Williams for early support of this work, B. Buisson for discussions, and G. R. Dick for discussions and reagents. N.J.C. is supported by a National Science Foundation Graduate Research Fellowship Program fellowship. A.B. is supported by the Pew Foundation. M.P. is supported by the Pew Program in Biomedical Sciences, the Terman Fellowship, Keck Foundation, the Gordon and Betty Moore Foundation and a National Science Foundation Career Grant.

Author Contributions N.J.C. made the original observation. All authors designed the research. N.J.C. and A.B. conducted experiments, and all authors interpreted the data; N.J.C. and A.B. developed the models. N.J.C and A.B. wrote the manuscript, and all authors commented on it.

Author Information Reprints and permissions information is available at www.nature.com/reprints. The authors declare no competing financial interests. Readers are welcome to comment on the online version of the paper. Correspondence and requests for materials should be addressed to M.P. (manup@stanford.edu).

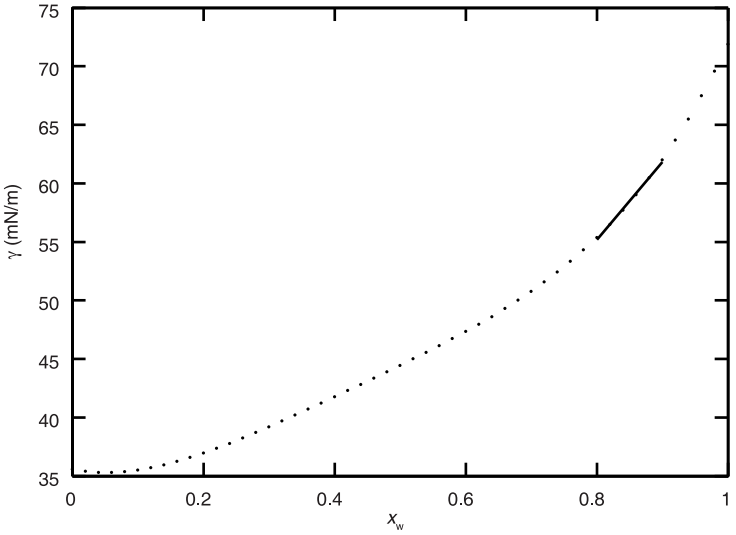

Extended Data Figure 1 | Surface tension γ_{LV} of PG/water mixtures as a function of mass fraction of water, x_w. Data extracted from ref. 27. We used the fourth-order polynomial, $\gamma_{LV} = 113x^4 - 192.27x^3 + 126.57x^2 - 11.69x + 35.6$ to fit this data. The data are fitted well by a linear function for a water fraction between 0.8 and 0.9.

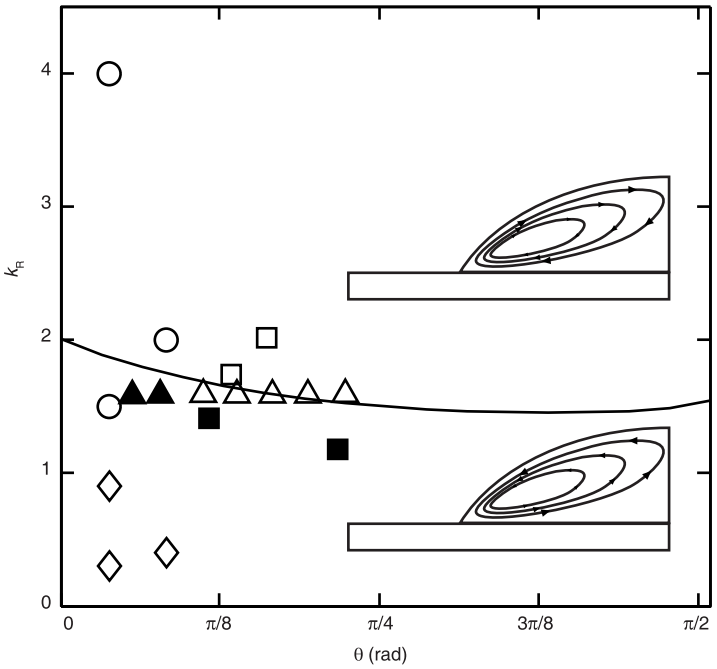

Extended Data Figure 2 | Conductivity ratio k_R versus contact angle θ. Data extracted from ref. 32. k_R indicates the ratio of conductivities between the substrate and liquid. Above the solid line, thermocapillarity is expected to drive flow clockwise in the half-droplet shown (upper inset), while below the solid line thermocapillarity predicts a counterclockwise flow (lower inset). Open symbols indicate clockwise flow and closed symbols indicate counterclockwise flow. Squares (from ref. 32) indicate chloroform, isopropanol, ethanol, and methanol on poly(dimethylsiloxane); triangles (from ref. 19) indicate water on glass; circles (this work) show PG/water on glass slides; and diamonds (this work) show PG/water on ITO/PET substrates. In our system we sample a space above and below this separation line, yet we observe flow only in one direction, which indicates that thermocapillarity is not the dominant effect. (See Supplementary Information section 2.5.)

32. Ristenpart, W. D., Kim, P. G., Domingues, C., Wan, J. & Stone, H. A. Influence of substrate conductivity on circulation reversal in evaporating drops. *Phys. Rev. Lett.* **99,** 234502 (2007).

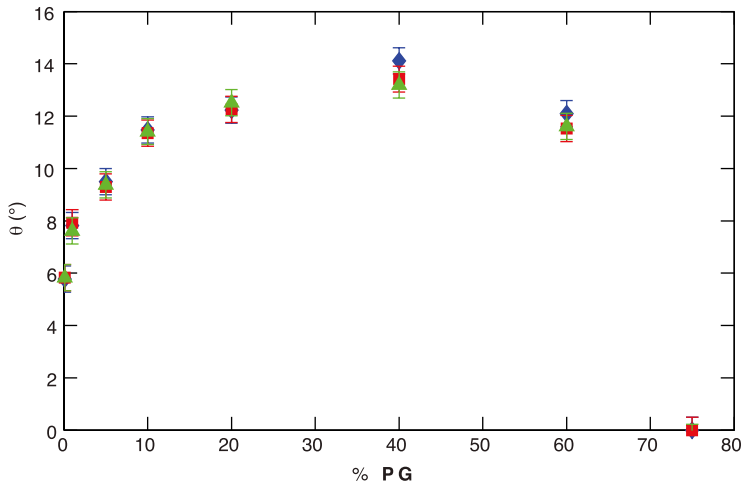

Extended Data Figure 3 | Contact angle of PG/water mixtures on surfaces of various conductivities. We measured contact angle by reflectometry on corona-discharge-cleaned glass slides (green triangles), corona-discharge-cleaned glass coverslips (136 μm thickness, red squares), and plasma-oven-treated ITO/PET (blue diamonds). If thermocapillarity were the only driving force for droplet stabilization the droplet would be predicted to spread on the ITO/PET. If thermocapillarity had a detectable role in stabilizing the droplets then we would expect to measure different contact angles for our droplets on these different substrates. (See Supplementary Information section 2.5.) Error bars are the range of three measurements at 75% RH.

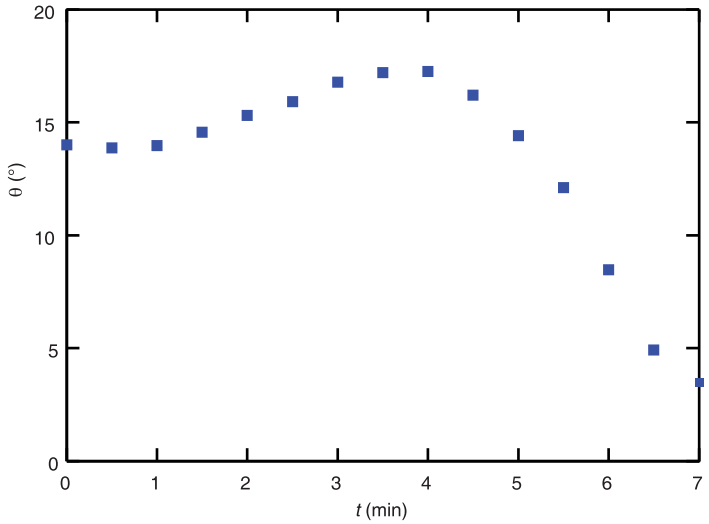

Extended Data Figure 4 | Contact angle change with time for a 0.5 µl 10% PG droplet at 30% RH. Contact angle changes very little at the minute scale. Over longer timescales as evaporation occurs, the volume fraction of PG in the bulk droplet becomes higher and the equilibrium contact angle changes to reflect the new concentration. The rate of evaporation sets a limit for the duration of the effects.

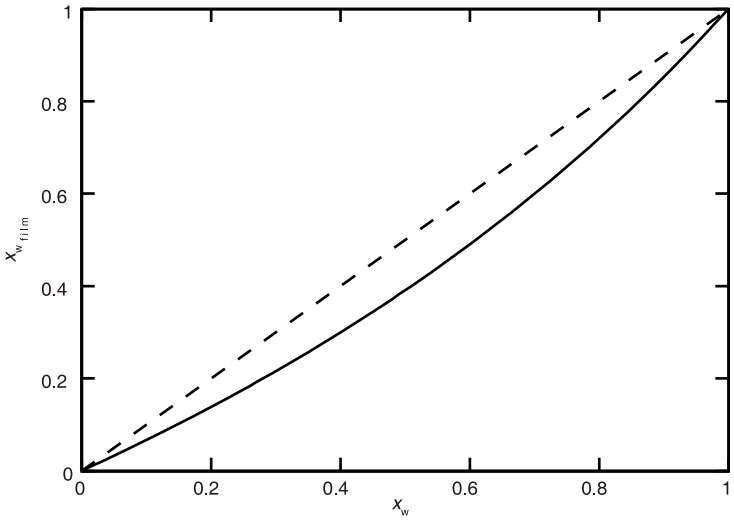

Extended Data Figure 5 | Film water volume fraction (solid line) as a function of the droplet volume fraction at 40% RH as predicted by our model. The dotted line is added to highlight the bulk droplet fraction. The difference between these lines is the concentration difference between the droplet and the thin film.

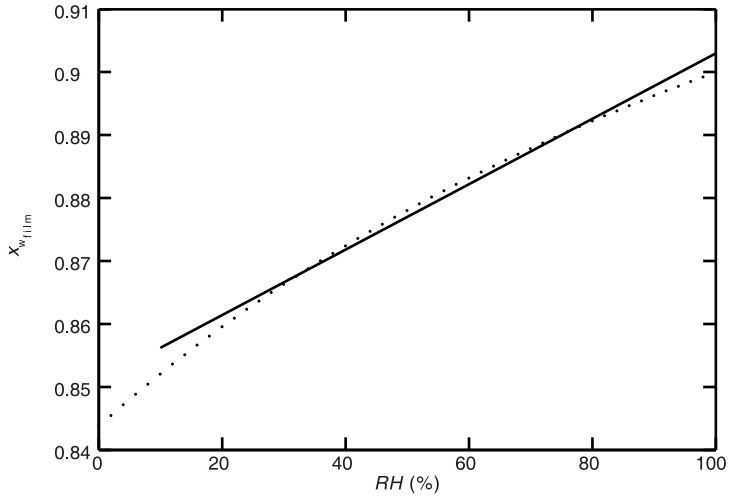

Extended Data Figure 6 | Film water volume fraction as a function of external humidity. Data shown for a 10% PG droplet as predicted by the model (dotted line). Note that over this range the variation can be approximated as a linear function (solid line).

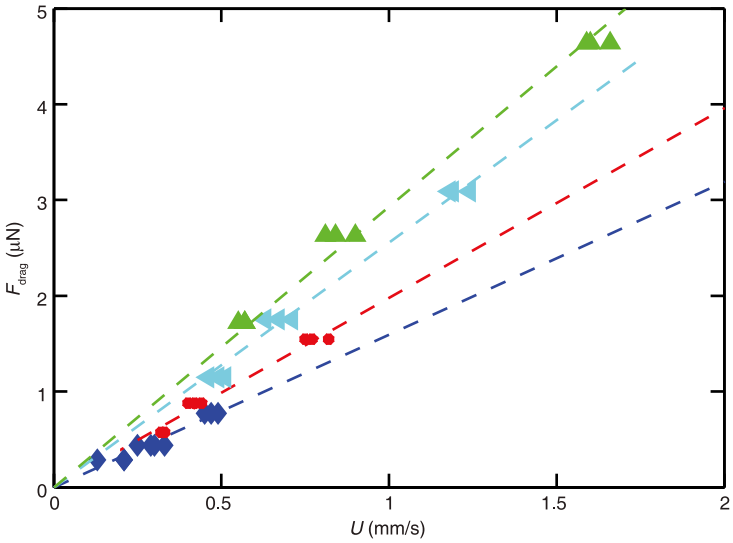

Extended Data Figure 7 | Drag force F_{drag} as a function of velocity U. Shown for 10% PG droplets of 0.25 μl (blue), 0.5 μl (red), 1 μl (cyan), 1.5 μl (green). The dashed lines represent the best linear fits.

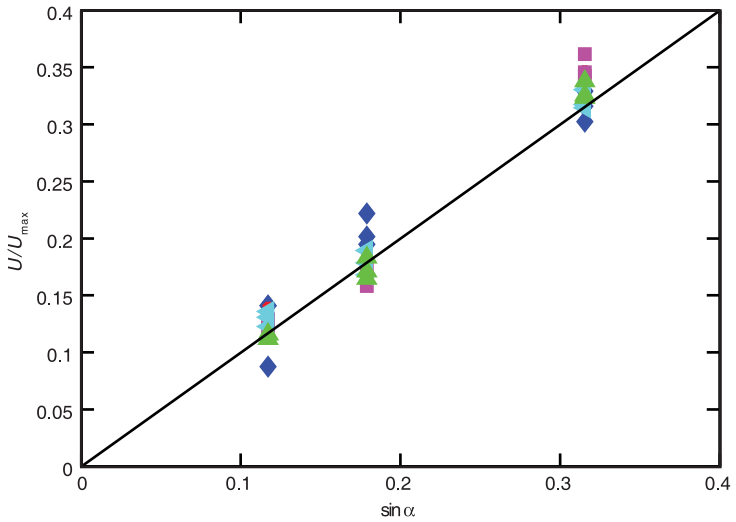

Extended Data Figure 8 | U/U_{max} as a function of sinα. Shown for the cutoff constant, $l_n = 11.2$, for 10% PG droplets of 0.25 µl (blue), 0.5 µl (red), 0.75 µl (magenta), 1 µl (cyan), 1.5 µl (green). The solid line represents the theoretical relation presented in the 'Drag coefficient theory' section (Supplementary Information section 2.1).

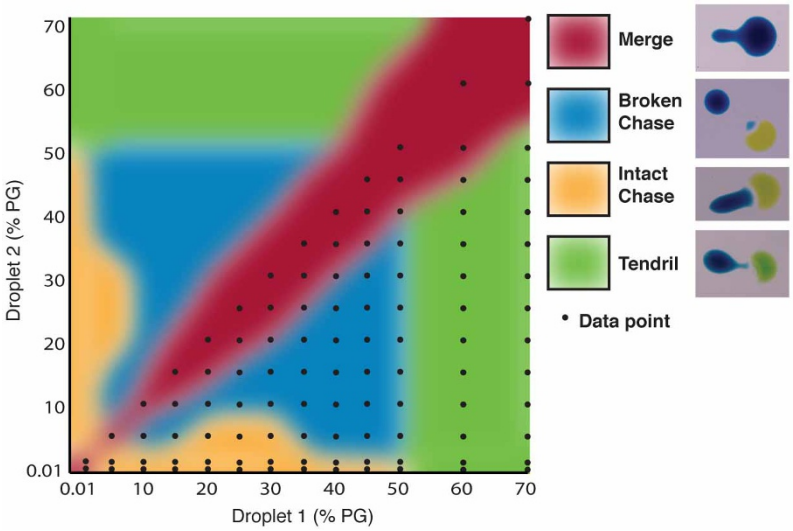

Extended Data Figure 9 | Phase plot of the short-range droplet interactions. 0.5 µl droplets of various concentrations. Each black dot indicates an experiment. Four qualitatively different regions are represented by colours and defined in the upper right. Exact boundaries between these regions are not always sharp.

Extended Data Table 1 | Behaviour of two-component chemical mixtures

	water	glycerol	ethylene glycol	1,3-butanediol	PG	DMSO	TPG	p-dioxane	DPGME	acetic acid	acetone	methanol	ethanol	IPA	1-propanol	pyridine	formic acid	ethanol amine	DMF	furfuryl alcohol	morpholine
Vapour pressure (mm Hg)	24	0.0002	0.08	0.06	0.15	0.6	0.01	37	0.4	16	231	127	59	45	21	21	45	0.4	3.3	0.8	10
Surface tension (mN/m)	73	64	48	47	36	43	30	33	28	27	23	22	22	23	21	37	38	48	34	53	39
water	2	1	1	1	1*	1	1	2	1	5	2	2	2	2	2	5	5	5	1	1	1
glycerol		2	2	2	2	2	2	2	2	2	5	2	2	2	2	5	2	2	2	2	2
ethylene glycol			2	2	2	2	5	2	2	2	5	2	2	2	2	2	2	2	2	2	2
1,3-butanediol				2	2	2	5	2	2	2	5	2	2	2	2	2	2	2	2	5	2
PG					2	2	5	2	2	2	5	2	2	2	2	2	2	2	2	5	2
DMSO						2	2	2	2	5	2	2	2	2	2	2	5	2	2	2	2
TPG							2	2	2	2	5	2	2	2	2	1	1	1	1	1	1
p-dioxane								5	1	5	2	2	2	2	1	2	5	2	2	2	2
DPGME									2	2	2	2	2	2	2	1	1	1	1	1	1
acetic acid										2	2	2	2	2	2	5	5	5	2	5	5
acetone											2	2	2	2	2	2	2	2	2	2	2
methanol												2	2	2	2	2	2	2	2	2	2
ethanol													2	2	2	2	2	2	2	2	2
IPA														2	2	2	2	2	2	2	2
1-propanol															2	2	1	2	2	2	2
pyridine																2	5	2	2	2	2
formic acid																	2	5	5	5	5
ethanol amine																		2	2	2	2
DMF																			2	5	2
furfuryl alcohol																				2	5
morpholine																					2

The table shows the behaviour of various two-component chemicals on clean glass. Chemicals were mixed in equal volume ratios and 0.5 μl of this mixture was placed on a treated glass slide. '1' indicates a droplet was formed. '2' indicates the mixture spread. '5' indicates a reaction is possible (for example, acid/base reactions are possible with water and formic acid), or the result was not clear (for example, the high viscosity of tripropylene glycol made some assessments difficult). Chemical vapour pressures and surface tensions were taken from various sources including vendors and published values. The asterisk indicates the water/PG mixture characterized in detail here. For abbreviations, see Supplementary Information section 1.3.